Acta metall. Vol. 37, No. 7, pp. 2077–2084, 1989
Printed in Great Britain

0001-6160/89 $3.00 + 0.00
Pergamon Press plc

OBSERVATIONS AND ANALYSIS OF SINTERING DAMAGE

C. P. OSTERTAG, P. G. CHARALAMBIDES and A. G. EVANS
Materials Department, College of Engineering, University of California, Santa Barbara, CA 93106, U.S.A.

(*Received* 11 *July* 1988)

Abstract—The influence of differential shrinkage on sintering damage induced by initially dense cylindrical heterogeneities has been examined. Radial cracks, formed at the matrix/inhomogeneity interface constitute the dominant mode of sintering damage. Sequential damage observations around the inhomogeneity have revealed an increase in crack-length and crack-opening displacement with increasing initial density differential between the matrix and the inhomogeneity. The stresses responsible for the crack-like damage have been estimated from viscosity data and unconstrained shrinkage rates obtained on the porous matrix at different temperatures and porosities. Correlations between theory and experiment are discussed.

Résumé—On examine l'influence de la contraction différentielle sur les dommages de frittage dus à des hétérogénéités cylindriques initialement denses. Des fissures radiales, formées à l'interface matrice–hétérogénéité constituent le mode dominant du dommage de frittage. Des observations d'endommagement séquentiel autour de l'hétérogénéité révèlent un accroissement de la longueur de fissures et du déplacement de l'ouverture de fissures quand on accroît la différence de densité initiale entre la matrice et l'hétérogénéité. Les contraintes responsables de l'endommagement par fissuration ont été évaluées à partir de données de viscosité et des taux de contraction sans contrainte obtenus sur la matrice poreuse à différentes températures et porosités. On discute les corrélations entre la théorie et l'expérience.

Zusammenfassung—Der Einfluß der differentiellen Schrumpfung auf die Sinterschädigung, hervorgerufen durch anfänglich dichte zylindrische Heterogenitäten, wird untersucht. Radiale Risse bilden sich an der Grenzfläche der Heterogenität zur Matrix und stellen die vorherrschende Art der Sinterschädigung dar. Beobachtungen des Verlaufes der Schädigung um die Inhomogenitäten herum zeigen, daß Rißlänge und Rißöffnung größer werden, wenn die anfängliche Dichtedifferenz zwischen Matrix und Inhomogenität ansteigt. Die Spannungen, die für die rißähnliche Schädigung verantwortlich sind, wurden aus der Viskosität und den uneingeschränkten Schrumpfungsraten, die an der porösen Matrix bei verschiedenen Temperaturen und Porositätsgraden erhalten wurden, ermittelt. Der Zusammenhang zwischen Theorie und Experiment wird diskutiert.

1. INTRODUCTION

Heterogeneities in a sintering compact induce stresses [1–8] when shrinkage rate differential exists. The stresses are influenced by the net driving force for sintering (the sintering potential), the creep viscosity of the constituents and the shape and number density of heterogeneities [4]. The stresses may be calculated provided that adequate constitutive laws describing the variations in viscosity and densification exist. Such calculations reveal that circumferential tensile stresses develop around initially dense heterogeneities. It has thus been suggested that sintering damage is most likely to occur in association with hereogeneities of this type [4]. It is the intention of the present study to examine sintering damage induced by such heterogeneities.

In order to obtain an adequate fundamental understanding of sintering damage mechanisms, it is important to be able to trace the evolution of specific damage entities at various stages in their development. Surface connected heterogeneities are required for this purpose (Fig. 1). The presence of the surface results in a substantially more complex stress state than previously analyzed. Nevertheless, numerical solutions can be obtained. Furthermore, the results are directly relevant to effects that obtain in fiber composites made by sintering.

Densification and creep experiments have been used to provide the parameters applicable to the constitutive behavior of partially sintered MgO. These results have been used in conjunction with a *finite element* scheme to calculate sintering induced stresses in and around the heterogeneity. Finally, stress intensity factors and creep crack growth rates have been estimated, as needed to provide comparisons between theory and experiment.

2. DAMAGE OBSERVATIONS

2.1. Experimental procedures

The experiments have been conducted using MgO with 98.8% purity and a 1 μm mean particle size. Cylindrical heterogeneities (0.6 cm in radius) have been fabricated from the MgO powder by either hot pressing or isostatic cold pressing followed by

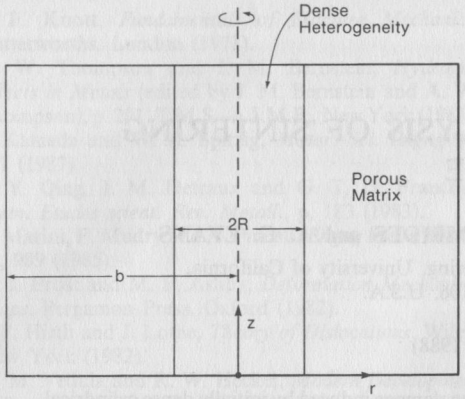

Fig. 1. Cylindrical geometry used for differential sintering experiments.

sintering. The heterogeneities have subsequently been incorporated into a lower density host by locating them in the center of a loosely packed powder compact (consisting of the same MgO powder), followed by isostatic cold pressing.

A step-wise sequential sintering schedule has been selected (Fig. 2) in order to facilitate damage observations. The schedule entails sintering for 1 hour at each of four different temperatures, between 1250 and 1550°C. Substantial sintering rate differentials could thereby be imposed after completion of each 1-h cycle and trends in damage rapidly assessed. Selected isothermal tests have also been performed wherein specific time dependent trends were required.

2.2. *Damage evolution*

Radial cracks constitute the predominant mode of sintering damage (Fig. 3), although a shallow interface separation also occurs at the interface. Damage has been characterized in terms of the radial crack length and the crack opening displacement, measured after each sintering cycle using scanning electron micrographs. Following each sintering cycle, the new crack tip position was used as a reference for displacement measurements. Subsequent crack tip positions were then precisely related both to each other and to the distance from the

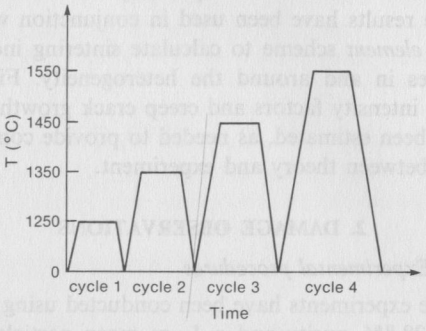

Fig. 2. Step-wise sequential sintering schedule. The schedule entails sintering for 1 h at each temperature with a heating rate and cooling rate of 10°C/min and 12°C/min, respectively.

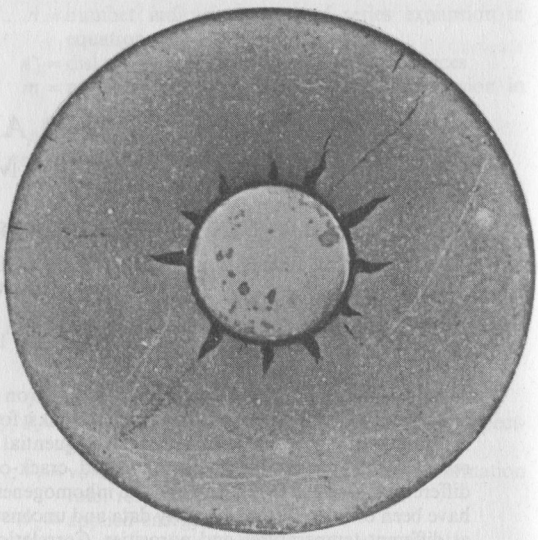

Fig. 3. SEM micrograph showing radial cracks formed after the final sintering cycle ($T = 1550$°C). Note that the cracks have a maximum opening at the interface.

interface (Table 1). Several important features are apparent. The crack opening displacements vary monotonically with temperature (Fig. 4). Furthermore, the temperature at which cracks first initiate is dependent upon the initial density differential, $\Delta\rho_0$. The systems having the largest $\Delta\rho_0$ exhibit crack formation at the lowest sintering temperature (1250°C): cracks cannot be generated below 1450°C for the system with the smallest $\Delta\rho_0$. After initial formation, the net crack length seemingly *decreases* upon sequential sintering. However, the relative radial shrinkage during the same period exceeds the increase in crack length. Consequently, on the basis of microstructural fudicial marks, the crack tip is found to advance during each cycle, as evident from the sequence depicted in Fig. 5. A representative measure of damage development is thus the

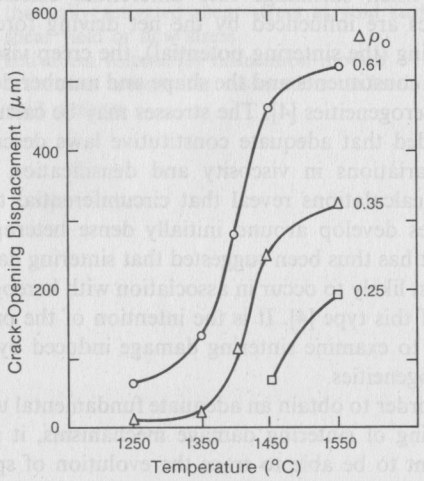

Fig. 4. Dependence of crack-opening displacement on differential density $\Delta\rho_0$. No cracks were observed below $T = 1450$°C when $\Delta\rho_0 = 0.25$.

Table 1. Trends in crack-opening and crack-length with initial density differential $\Delta\rho_0$ and temperature T

	1250°C		1350°C		1450°C		1550°C	
	a (μm)	u (μm)	a (μm)	u (μm)	a (μm)	u (μm)	a (μm)	u (μm)
$\Delta\rho_0 = 0.25$					360	64	220	196
$\Delta\rho_0 = 0.35$	730	6	620	16	510	250	470	310
$\Delta\rho_0 = 0.61$	1350	60	1250	170	1100	470	1080	540

a = crack-length.
u = crack-opening displacement.

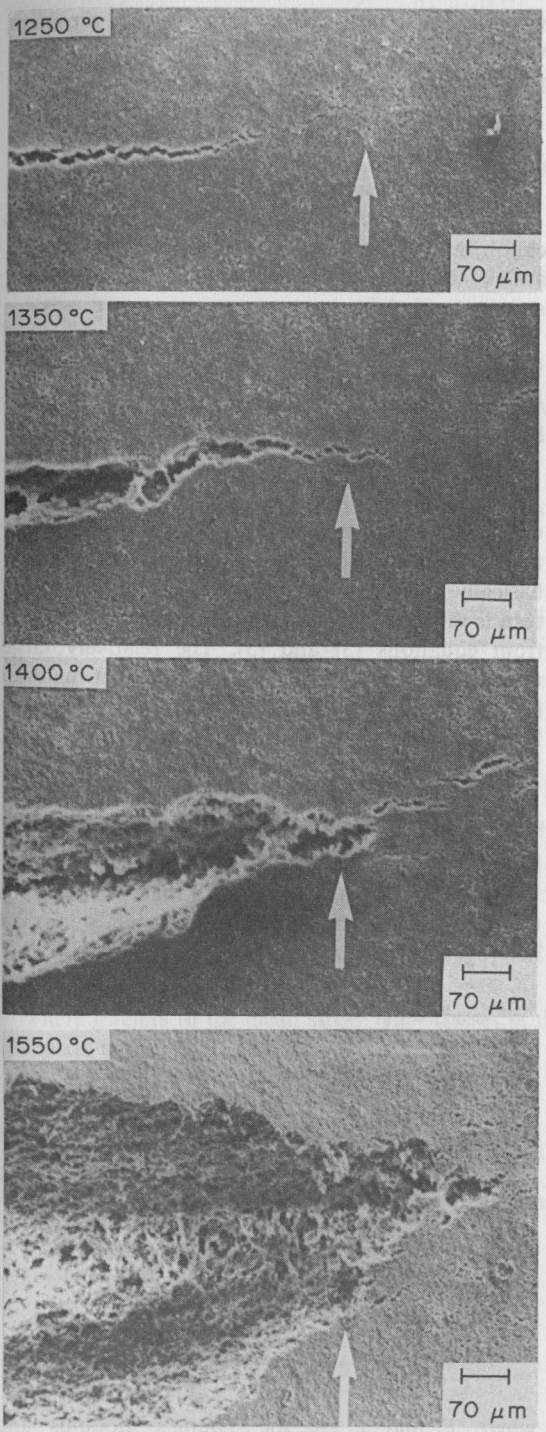

Fig. 5. SEM micrograph of a radial crack ($\Delta\rho_0 = 0.61$) at different temperatures. The crack initiates at $T = 1250$°C and advances with increasing sintering temperature, as shown by the fudicial marks.

sequential crack tip advance, Δa (Fig. 6). Trends in Δa indicate diminishing crack tip advance tendencies with increase in temperature.

Cross sectioning studies of selected specimens revelaed that the radial cracks exhibit an elliptical profile (Fig. 7), such that their surface extension exceeds their depth extension by ~ 3 in all instances. Evidently, therefore, near surface stress concentrations exert an important influence on crack development in this configuration.

3. CONSTITUTIVE BEHAVIOR

3.1. Unconstrained shrinkage rates

The unconstrained densification characterizations have been measured at different temperatures using standard dilatometry procedures. The results can be fitted to the density dependent constitutive law established in a prior study [4] (Fig. 8)

$$\rho = 1 - \frac{1 - \rho_0}{(1 + t/\tau)^{\beta}} \tag{1}$$

or

$$1 - \rho = \Delta\rho_0/(1 + t/\tau)^{\beta}$$

where ρ is the relative density, ρ_0 the density after 1 h sintering time at the *previous* temperature, t the sintering time and β and τ are empirical parameters (Table 2). The paramter τ is temperature dependent

$$\tau \sim \exp[Q_g/kT] \tag{2}$$

where Q_g is the activation energy. Differentiation of equation (1) and incorporation of the sintering potential, Σ [4], gives the unconstrained densification-rate

$$\dot{\rho} = \frac{\beta(1-\rho)^{1+1/\beta}(1 - \bar{\sigma}/\Sigma)}{\tau \Delta\rho_0^{1/\beta}} \tag{3}$$

where $\bar{\sigma}$ is the mean stress.

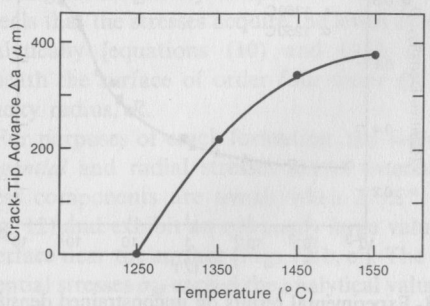

Fig. 6. Crack-tip advance tendencies with increasing temperature ($\Delta\rho_0 = 0.35$).

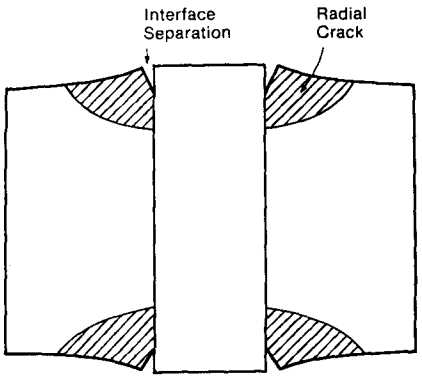

Fig. 7. Schematic profile of radial cracks.

3.2. *Viscosities*

Viscosity measurements of the stress relaxation type were performed on cylindrical samples. The experimental procedure is described in detail elsewhere [9]. Herein, the essential steps are briefly addressed. The load was increased to a predetermined peak value (1.2 MPa) and then allowed to relax at constant displacmeent. The variation in load with time was recorded. Densification during the tests was minimized by the selection of a small peak stress and by using only short duration results. The stress relaxation curves satisfy the Maxwell relation

$$\sigma(t) = \sigma_0 \exp\left(\frac{-tE}{\eta}\right) \tag{4}$$

where σ_0 is the peak stress (prior to relaxation) and E is the Young's modulus. Relative viscosities, η/E, have been determined by fitting the data to equation (4). The viscosities obtained using the above procedures are expressible in terms of a previously determined constitutive law [4] (Fig. 9).

$$\eta = \eta_0 \rho^p (1-\rho)^{-\lambda} \tag{5}$$

where p and λ are fitting parameters and η_0 is a temperature dependent parameter

$$\eta_0 \sim \exp Q_b/kT$$

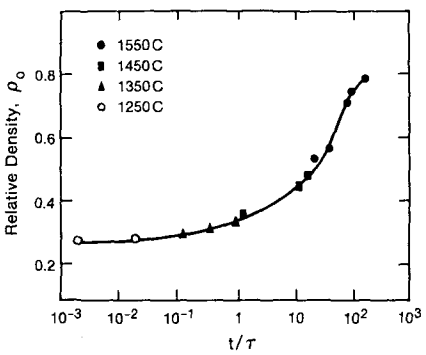

Fig. 8. Experimental results on unconstrained densification at different temperatures, fitted to the density dependent law, derived by Hsueh *et al.* [4].

Table 2. Parameters of constitutive law for densification

T(°C)	$\tau(s)$	β
1250	15,600	0.2
1350	6,000	0.2
1450	720	0.2
1550	120	0.2

where Q_b is the activation energy for the prevalent viscous flow process. The operative values of these paramters are summarized in Table 3.

4. STRESSES

The viscoelastic stresses that develop upon densification can be calculated by combining equations (3) and (5) with expressions for the linear unconstrained strain-rate [3, 4, 8]

$$\dot{\epsilon} = -\dot{\rho}/3\rho \tag{6}$$

and the stress. In the viscous limit, the stress is given by [1, 8]

$$\sigma_{ij} = \eta \dot{\epsilon} g_{ij}(r, z) \tag{7}$$

where σ_{ij} is the stress and g_{ij} the spatial variation in the *elastic* field. Consequently, the stress levels are basically governed by the product $\dot{\rho}\eta$, which in turn is reflected in the parameter, $\beta\eta_0/\tau\Sigma$, as evident from equations (3) and (5). The relatively large magnitude of this parameter for the present material (Table 3) indicates that the stresses approach the bound governed by equation (3), viz.

$$\bar{\sigma}^m \to \Sigma. \tag{8}$$

The validity of this bound is further explored below.

Previous analysis has shown [7] that, remote from the free surface, the elastic stresses in the cylindrical heterogeneity are *uniform* and given by

$$\begin{aligned}\sigma_{rr}^h = \sigma_{\theta\theta}^h = \Bigg\{&(1-f) \\ &\times \left[(1-f)(1+\nu^h)\frac{E_m}{E^h} + f(1+\nu^m)\right] E^m \epsilon \Bigg\} \\ &\times \Bigg\{\left[(1-f)\frac{E^m}{E^h} + f\right] \\ &\times \left[(1-\nu^h)(1-f)\frac{E^m}{E^h} + (1+f) + \nu^m(1-f)\right] \\ &- 2\left[\nu^h(1-f)\frac{E^m}{E^h} + f\nu^m\right]^2\Bigg\}^{-1}\end{aligned} \tag{9}$$

where E and ν are the Young's modulus and Poisson's ratio respectively, ϵ is the unconstrained strain, f is the volume fraction of the heterogeneity and the superscripts m and h refer to the matrix and

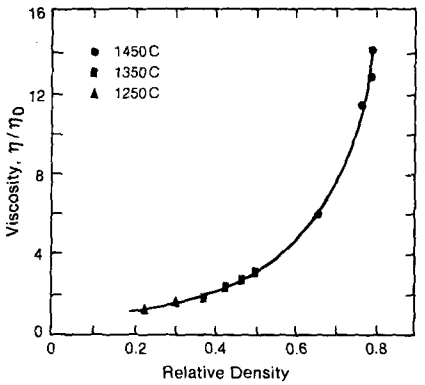

Fig. 9. Experimental results for viscosity fitted to a constitutive law developed by Hsueh *et al.* [4].

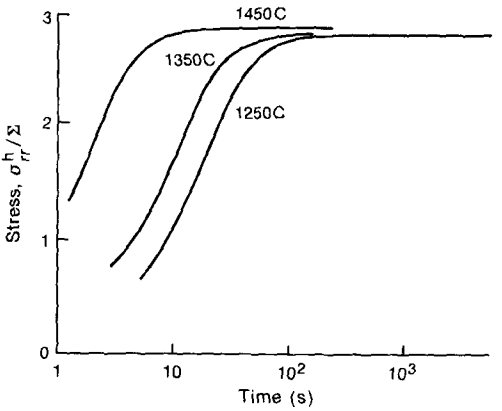

Fig. 10. Viscoelastic interfacial stresses calculated for different temperatures and an initial density differential, $\Delta\rho_0 = 0.5$, using the constitutive parameters from Tables 2 and 3 ($f = 0.05$).

heterogeneity, respectively. The corresponding axial stress is

$$\sigma^h_{zz} = \frac{(1-f)\left[(1-f)(1-\nu^h)\frac{E^m}{E^h}+1+f+\nu^m(1-f)+2\nu^h(1-f)\frac{E^m}{E^h}+2f\nu^m\right]E^m\epsilon}{\left[(1-f)\frac{E^m}{E^h}+f\right]\left[(1-\nu^h)(1-f)\frac{E^m}{E^h}+(1+f)+(1-f)\nu^m\right]-2\left[\nu^h(1-f)\frac{E^m}{E^h}+f\nu^m\right]^2}. \quad (10)$$

Consequently, for a dense heterogeneity ($E^h \to \infty$), for $\nu^m = 1/2$ (the viscous value) and equating $\eta\dot{\epsilon}$ to $G^m\epsilon$, equations (7), (9) and (10) give

$$g^h_{rr} = g^h_{\theta\theta} = 3(1-f) \quad (11a)$$

and

$$g^h_{zz} = 3(1-f^2)/f \quad (11b)$$

and therefore, the mean stress takes the form

$$\bar{g}^h = \frac{(1+3f)}{3f} g^h_{rr} \quad (11c)$$

such that

$$\bar{g}^m = -\frac{(1+3f)}{3(1-f)} g^h_{rr} \quad (12)$$

where $\bar{g}$ refers to the mean stress. The stresses in the matrix are [7]

$$g^m_{\theta\theta} = -g^h_{rr}[f+(R/r)^2]/(1-f)$$
$$g^m_{rr} = g^h_{rr}[(R/r)^2 - f]/(1-f) \quad (13)$$

where R is the heterogeneity radius and r the distance from the center.

Table 3. Fitting parameters of constitutive law for viscosity

T (°C)	η_0 (GPa·s)	p	λ	η_0/τ (GPa)
1250	3780	0.1	1.7	0.24
1350	1320	0.1	1.7	0.22
1450	540	0.1	1.7	1.3
1550	240	0.1	1.7	2.0

Note that Σ is of order 1 MPa, such that $\beta\eta_0/\tau\Sigma$ is of order 10^2.

Applying the bound expressed by equation (8), the stress predicted by equation (10) is

$$\sigma^h_{rr}/\Sigma = \sigma^h_{\theta\theta}/\Sigma = -3(1-f)/(1+3f). \quad (14)$$

This bound is close to the steady-state viscoelastic values calculated numerically (Fig. 10) and will thus be used for further analysis.

The stresses are much more complex near the surface where the radial cracks are observed to form. To determine these stresses, a finite element solution is developed, based on a thermal stress routine, using the ABAQUS code. The mesh employed as well as the boundary conditions are described in the Appendix. The finite element method has been used to generate salient features of the near surface stress field, as summarized in Figs 12 and 13. Of particular interest for present purposes are the stresses that obtain for large E^h/E^m. In this regard, it is firstly noted that the stresses are essentially invariant with the modulus ratio when $E^h/E^m > 10^2$. Results for $E^h/E^m \sim 10^3$ are thus representative of a rigid non-sintering heterogeneity. Inspection of Fig. 12 also reveals that the stresses acquire the levels determined analytically [equations (10) and (13)] at depths beneath the surface of order four times the heterogeneity radius, R.

For purposes of crack formation, the *near surface tangential* and radial stresses are of interest. Both stress components are *tensile* when E^h/E^m is large (Fig. 12) and exhibit an extremely large value at the interface near the surface [Figs 12(b, c)]. The circumferential stresses $\sigma_{\theta\theta}$ exceed the analytical value [equation (13)] over a radial zone equal to $\sim 0.25R$, while the radial stress is tensile over a small depth of order

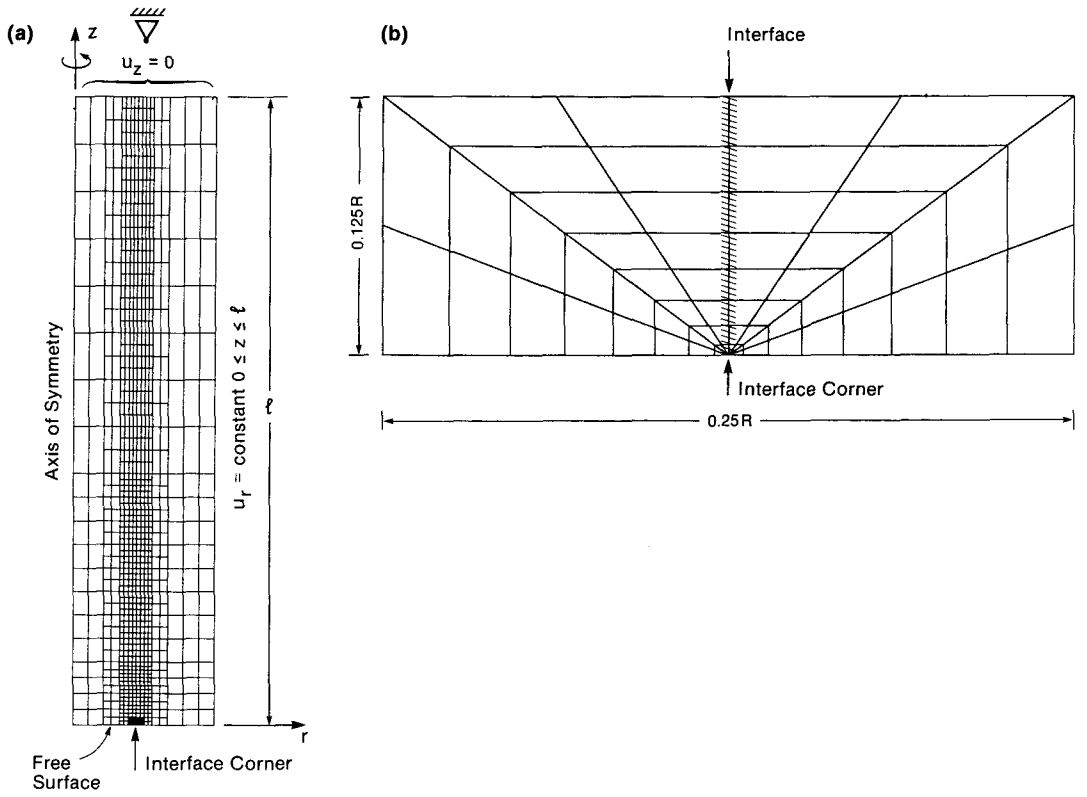

Fig. 11. The finite element mesh used to calculate the stresses near the surface.

$0.2R$. The implications for damage formation are discussed below.

5. DAMAGE ANALYSIS

The stress analysis of the preceding section can be used to rationalize various aspects of the damage observations. Firstly, it is noted that the very large radial and circumferential stresses at the surface near the interface are consistent with the ready *nucleation* both of radial cracks and of shallow interface separations. Indeed, the stresses are sufficiently large that material characteristics which completely suppress crack nucleation are unlikely. However, the avoidance of significant crack *extension* is probably of greater practical importance. Crack propagation in creeping linear materials is governed by a stress intensity factor, K [10]. Rigorous analysis of the K's associated with the radial cracks is beyond the scope of the present article. Instead, the stress intensity factors for a plane strain radial crack emanating from the heterogeneity are used to explore feasibility. For this purpose, it is noted that the radial cracks have a maximum opening at the interface (Fig. 3). A relevant solution is thus given by K for a crack of length $2a$ (measured from the center of the heterogeneity), subject to a stress $\sigma^h_{\theta\theta}$ acting over a length $2R$. This solution is [11]

$$K = -[2\sigma^h_{\theta\theta}/\sqrt{\pi}]\sqrt{a}\,\sin^{-1}(R/a) \tag{15a}$$

or from equation (14)

$$K/\Sigma\sqrt{a} = [6(1-f)/\sqrt{\pi}(1+3f)]\,\sin^{-1}(R/a). \tag{15b}$$

Inserting measured values for the crack length ($2a \approx 10$ mm) indicates that the K level for crack growth is ~ 0.1 MPa $\sqrt{m}$.† This level compares with a critical value K_c for dense MgO of ≈ 1 MPa $\sqrt{m}$. Creep crack growth is typically observed in the range $0.1 \lesssim K/K_c < 1$ [13, 14]. The present results are thus consistent with a damage process occurring by creep crack growth in the presence of sintering induced stresses.

Creep crack growth rates exhibit a temperature dependence governed by the creep viscosity of the material [10, 13]. The observed increase in crack growth with increase in temperature (Fig. 6) can be attributed to this velocity effect, since K is essentially temperature independent. The trends in crack opening rate, $\dot{u}$, also have a dependence on viscosity [14]

$$\dot{u} \sim (K\sqrt{a}/\eta) \tag{16}$$

such that, upon inserting K from equation (15) and η from equation (5), the opening rate becomes

$$\dot{u}/a \sim \Sigma(1-\rho)^\lambda/\eta_0\rho^p. \tag{17}$$

This relation allows the data presented on Fig. 4 to be rationalized. The strong effect of *temperature* is

†Σ is assumed to be of order 1 MPa [12].

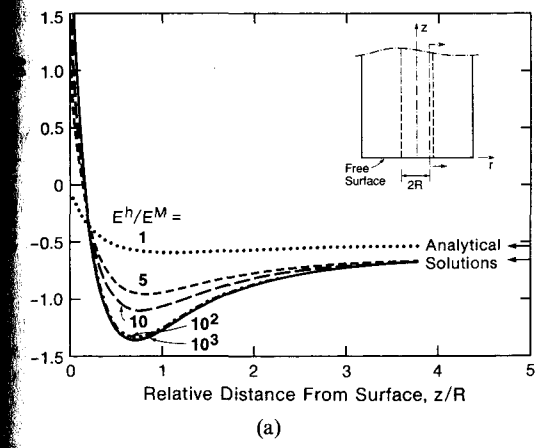

(a)

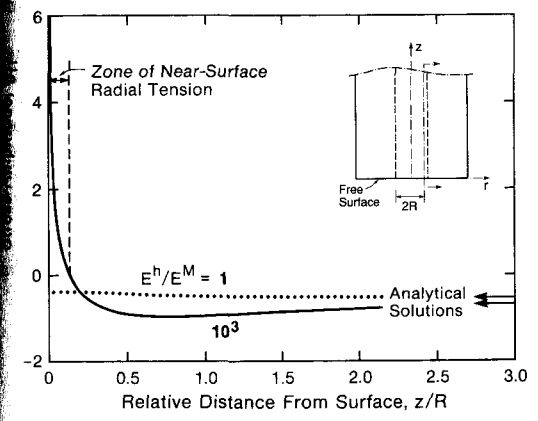

(b)

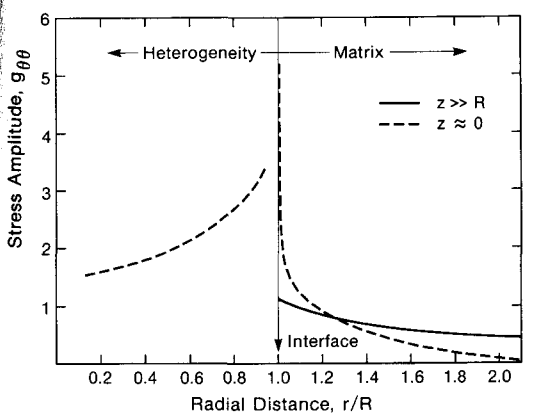

(c)

Fig. 12. Near surface elastic stresses calculated using finite elements for $f = 0.2$. (a) Circumferential stress at the interface: trends with distance from the surface. (b) Radial stress at interface: trends with distance from the surface. (c) Circumferential stress just beneath the surface ($Z \approx 0$): also shown is the stress in the matrix at $Z \gg R$.

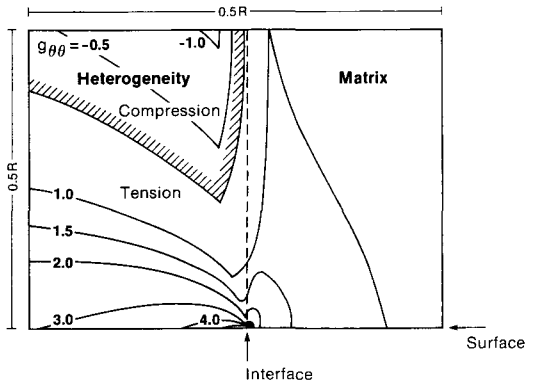

(a)

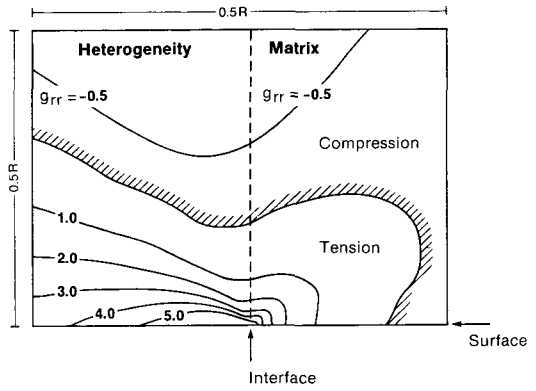

(b)

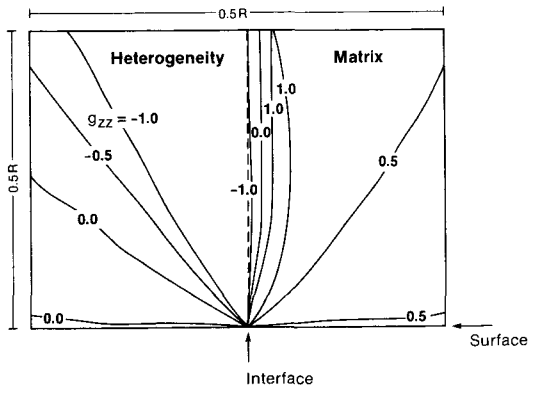

(c)

Fig. 13. Stress contours in the near surface region. (a) Circumferential. (b) Radial. (c) Axial.

governed by the temperature dependence of η_0 as apparent from Table 3. The effect of *density* (Fig. 4) is also consistent with equation (17) upon appreciating that the density difference $\Delta\rho_0$ reflects differing values of the matrix density ρ, such that $\rho \approx 1 - \Delta\rho_0$; whereupon, the variation in $\dot{u}$ with density has the form

$$\dot{u} \sim \Delta\rho_0^{1.7}(1 - \Delta\rho_0)^{0.1} \tag{18}$$

which agrees reasonably well with the measured values (Fig. 4).

6. CONCLUDING REMARKS

The constitutive properties of the sintering MgO powder, coupled with the existence of heterogeneity induced stresses, seemingly account for cracks observed during the sintering of a cylindrical body

containing a central, dense heterogeneity. Crack damage induced by the sintering stresses is consistent with the creep crack growth characteristics of the porous partially sintered material. Specifically, the rate of crack growth increases with increase in temperature and the crack opening rate is larger in more porous bodies, because of their lower viscosity. A more quantitative comparison between theory and experiment would require that creep crack growth characteristics in porous bodies be established as functions of porosity and temperature.

REFERENCES

1. A. G. Evans, *J. Am. Ceram. Soc.* **65,** 497 (1982).
2. B. J. Kellet and F. F. Lange, *J. Am. Ceram. Soc.* **67,** 369 (1984).
3. R. Raj and R. K. Bordia, *Acta metall.* **32,** 1003 (1984).
4. C. H. Hsueh, A. G. Evans, R. M. Cannon and R. J. Brook, *Acta metall.* **34,** 927 (1986).
5. C. H. Hsueh, *J. Am. Ceram. Soc.* **21,** 2067 (1986).
6. C. H. Hsueh, A. G. Evans and R. M. McMeeking, *J. Am. Ceram. Soc.* **69,** C64 (1986).
7. C. H. Hsueh, *Scripta metall.* **19,** 977 (1985).
8. R. K. Bordia and G. Scherer, *Acta metall.* In press.
9. C. P. Ostertag, Ph.D. thesis, Univ. of California at Berkeley (1985).
10. A. G. Evans and B. J. Dalgleish, *Ceram. Engng Sci.* **7,** 1073 (1986).
11. G. C. Sih, *Handbook of Stress Intensity Factors*, Lehigh Univ. Press (1973).
12. L. DeJonghe, L. Rahaman and C. H. Hsueh, *Acta metall.* **34,** 1467 (1986).
13. M. D. Thouless, *Res. Mechanica* **22,** 213 (1987).
14. W. Blumenthal and A. G. Evans, *J. Am. Ceram. Soc.* **67,** 751 (1984).

APPENDIX

The Finite Element Calculations

The specimen geometry under consideration is depicted in Fig. 1. During straining, the axi-symmetry of the problem is preserved. Therefore, the Finite Element equations need to be solved only in the one half of the unit cell region. The boundary value problem is thus reduced to that depicted in Fig. 11. The boundary conditions shown in the above figure enforce symmetry of the unit cell and compatible motion with its neighboring cells.

The finite elements used in the analysis were 8-noded, axisymmetric and isoparametric with 4-stations for the integration of the element stiffness. As shown in Fig. 11, a relatively coarse mesh was used away from the free surface and interface, whereas the region at the interface corner was finely discritized using the focused mesh depicted in the above figure. A total of 956 elements were used with 64 in the interface corner region.

The Poisson's ratio for both materials was set to be $v_f = v_m = 0.5$. The imposed loading was such that $E^m\epsilon > 0$.